



Intense upper ocean mixing due to large aggregations of spawning fish

Bieito Fernández Castro^{1,2}✉, Marian Peña³, Enrique Nogueira⁴, Miguel Gilcoto², Esperanza Broullón⁵, Antonio Comesaña⁵, Damien Bouffard⁶, Alberto C. Naveira Garabato¹ and Beatriz Mouríño-Carballido⁵

Small-scale turbulent mixing plays a pivotal role in shaping ocean circulation and a broad range of physical and biogeochemical processes. Despite advances in our understanding of the geophysical processes responsible for this mixing, the nature and importance of biomixing—turbulent mixing caused by marine biota—are still debated. A major source of uncertainty pertains to the efficiency of biomixing (the fraction of the turbulent energy produced through swimming that is spent in mixing the ocean vertically), which the few *in situ* observations available suggest to be much lower than that of geophysical turbulence. Here we shed light on this problem by analysing 14 days of continuous measurements of centimetre-scale turbulence in an area of coastal upwelling. We show that turbulent dissipation is elevated 10- to 100-fold (reaching 10^{-6} – 10^{-5} W kg $^{-1}$) every night of the survey due to the swimming activity of large aggregations of anchovies that gather regularly over the spawning season. Turbulent mixing is invigorated concurrently with dissipation, and occurs with an efficiency comparable to that of geophysical turbulence. Our results demonstrate that biologically driven turbulence can be a highly effective mixing agent, and call for a re-examination of its impacts on productive upper ocean regions.

Turbulence is a fundamental component of the ocean's energy budget, as it mediates the transfer of kinetic energy from large (1–1,000 km) to small (0.1–1 cm) scales, where such energy is dissipated as heat by molecular viscosity¹. However, dissipation is just one of two possible fates of turbulent kinetic energy (TKE). As turbulent motions stir the water column, microscale physical and chemical gradients are generated, and ultimately eroded, by molecular diffusion, resulting in mixing. When acting on a stable density profile, such as the oceanic pycnocline, turbulent mixing drives the upward transport of mass, and hence transforms a fraction of the TKE into potential energy². This fraction, referred to as the mixing efficiency, is relatively uncertain and challenging to quantify *in situ*. Observations and idealized simulations indicate that the mixing efficiency often approaches a value of ~0.16 (refs. ^{3,4}), as is characteristic of shear instabilities (a major source of ocean turbulence^{5,6}), yet there is mounting evidence that the mixing efficiency may vary extensively⁷.

The debate surrounding mixing efficiency is particularly relevant for appraising the relevance of biomixing⁸. Although winds and tides undeniably constitute the major sources of energy for ocean mixing on a global scale⁹, it has been suggested^{10,11} that swimming organisms (from zooplankton to fish and marine mammals) may also contribute a substantial energy input¹², at least on regional scales¹³. The relevance of this suggestion was initially endorsed by dynamical¹³ and metabolic¹⁴ considerations, laboratory experiments¹⁵ and early observations of elevated TKE dissipation (~ 10^{-5} W kg $^{-1}$) in fish aggregations¹⁶ and migrating krill swarms¹⁷. However, subsequent studies found biophysical turbulence extremely challenging to capture in lakes and oceans, indicating that this phenomenon might be rarer than originally thought^{18–21}. Furthermore, what little evidence exists of mixing produced by biophysical turbulence suggests that

the mixing efficiency of such turbulence is very low (<0.01) relative to that of geophysical, shear-driven turbulence. This evidence is based on the concurrent measurement of the rates of dissipation of TKE (ε , a measure of the intensity of turbulence) and of thermal variance (χ , a measure of the intensity of mixing)—quantified from observations of centimetre-scale velocity and temperature gradients, respectively—in the presence of swimming organisms^{16,19,21–23}. Only two of these investigations reported high ε levels within fish aggregations^{22,23} but, in both cases, these were associated with low values of χ ; that is, weak mixing. Thus, the present balance of evidence points towards the old-proposed view of an important large-scale influence of biomixing being unlikely.

Here, we contest and redress this balance by demonstrating the occurrence of recurrent, intense and efficient biomixing in an embayment affected by wind-driven coastal upwelling pulses (Ría de Pontevedra, Northwest Iberia; Extended Data Fig. 1)^{24,25}. This demonstration rests on the analysis of a two-week dataset of highly (temporally and vertically) resolved observations of hydrographic properties, turbulent dissipation and mixing rates, and acoustic backscatter (an indicator of fish and plankton density). The data were acquired during the REMEDIOS cruise in the summer of 2018 in three sampling periods (I01, 1–5 July; I02, 6–8 July; and I03, 9–13 July; see Methods for details of the dataset), and captured intense biophysical turbulence in every segment of the nocturnal measurements. This allowed an extremely detailed characterization of biophysical turbulence, its mixing efficiency and its biological underpinning.

Hydrographic and turbulence environments

The Ría's hydrographic setting varied notably during the measurement campaign, evolving from a downwelling to an upwelling

¹Ocean and Earth Science, National Oceanography Centre, University of Southampton, Southampton, UK. ²Departamento de Oceanografía, Instituto de Investigaciones Mariñas (IIM-CSIC), Vigo, Spain. ³Centro Oceanográfico de Baleares (IEO, CSIC), Palma de Mallorca, Spain. ⁴Centro Oceanográfico de Vigo (IEO, CSIC), Vigo, Spain. ⁵Centro de Investigación Mariña, Universidade de Vigo, GOB, Vigo, Spain. ⁶Eawag, Surface Waters - Research and Management, Swiss Federal Institute of Aquatic Science and Technology, Kastanienbaum, Switzerland. ✉e-mail: b.fernandez-castro@soton.ac.uk

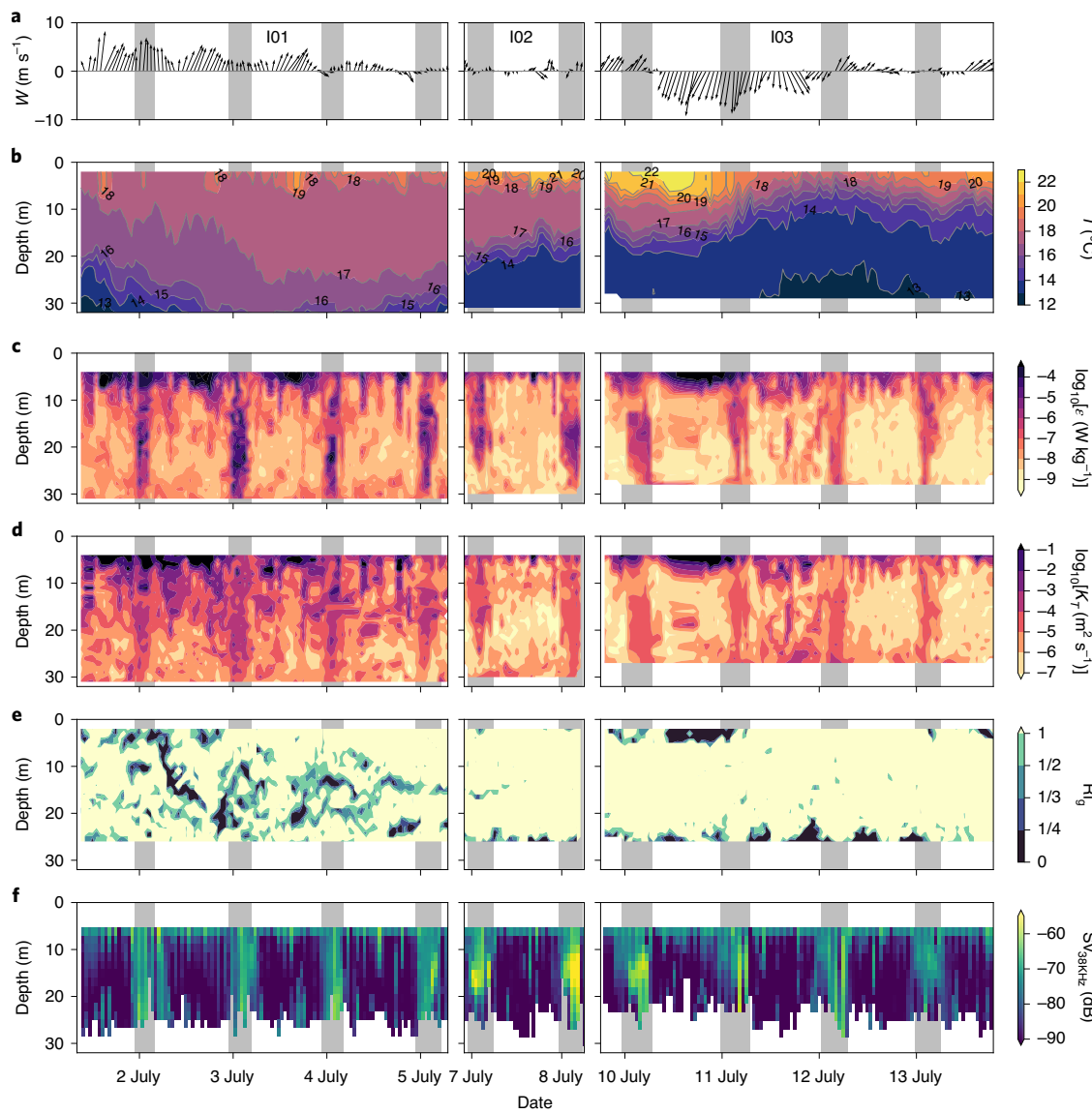


Fig. 1 | Hydrography, turbulence and mixing during the REMEDIOS survey. **a–f**, Time series of local wind speed (W) and direction measured at Cape Udra (Extended Data Fig. 1) (**a**), hourly mean T (**b**), ε (**c**), turbulent heat diffusivity (**d**), gradient Richardson number (**e**) and volume backscattering strength at 38 kHz (**f**) during I01, I02 and I03. Grey shading indicates night-time periods of enhanced biophysical turbulence. These periods were determined by inspection of the turbulent dissipation rate and volume backscattering strength records. The time axis is GMT (local time = GMT + 2 h). Note the use of logarithmic colour scales in **c** and **d**.

circulation over the fortnight of observations (Fig. 1a,b). In I01, southerly, downwelling-favourable winds were dominant (Fig. 1a) and thermal stratification was relatively weak (Fig. 1b), as a result of the import of surface shelf waters with a uniform temperature (T) of $\sim 17^{\circ}\text{C}$ into the embayment. After 4 July, calm conditions prevailed, and the circulation pattern reversed (Extended Data Fig. 2). During I02, relatively cold waters ($T \approx 13^{\circ}\text{C}$) upwelled into the Ría's deeper layers, giving rise to a stratified interface at ~ 20 m. The inflow of warmer and fresher waters produced an additional near-surface (< 10 m) stratified layer (Fig. 1b). At the outset of I03, strong northerly winds led to an intensification of cold-water upwelling, which brought about a single highly stratified layer.

The evolution of the Ría's turbulence environment bore little imprint of the hydrography, hinting at a non-physical origin of the turbulence. Thus, turbulent dissipation was recurrently enhanced over the entire water column every day after sunset and for a period

of 5–6 h (Fig. 1c). This enhancement (termed night-time dissipation hereafter) was most striking in the embayment's interior layers (10–25 m), away from the direct influence of wind-induced and bottom boundary turbulence. Within this depth interval, night-time ε was elevated by 1–3 orders of magnitude above background daytime values of 10^{-9} – 10^{-8} W kg^{-1} , reaching 10^{-7} – 10^{-5} W kg^{-1} (Fig. 1c and Extended Data Table 1). Background ε levels were higher during I01 (mean 1.22×10^{-7} W kg^{-1}) compared with I02 (1.71×10^{-8} W kg^{-1}) and I03 (2.17×10^{-8} W kg^{-1}). Night-time dissipation rates also decreased between I01 (mean 1.62×10^{-5} W kg^{-1}) and I02–I03 (1.96×10^{-6} and 0.82×10^{-6} W kg^{-1} , respectively).

Sources of turbulence

To assess the energy sources of the turbulence in the Ría, we first examined the extent to which geophysical factors might explain the measured dissipation patterns. Geophysical turbulence in

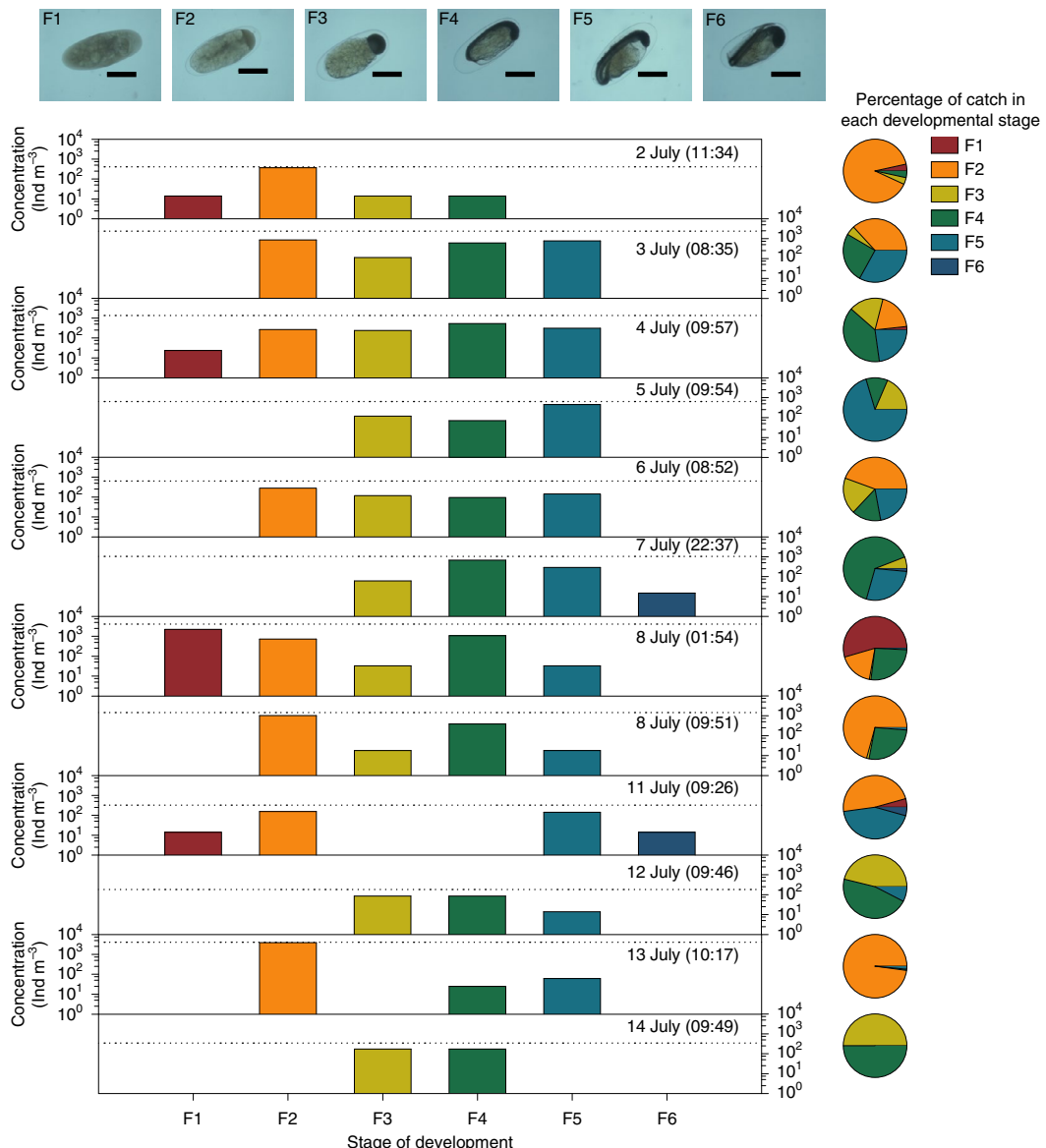


Fig. 2 | Anchovy egg concentrations. The number of individuals per cubic metre (Ind m^{-3}) at different development stages (F1 to F6; Extended Data Table 2) is shown for the time series of plankton net hauls carried out at the sampling location. The date and hour of sampling (GMT, local time = GMT + 2), and the total number of eggs (horizontal dotted line) are shown in each bar plot. The y axes are displayed on logarithmic scales. The pie charts indicate the percentages of eggs at the development stages considered, relative to the total number of eggs in each sample. The scale bars in each egg image are 0.5 mm. The average elapsed times since spawning corresponding to the different development stages according to ref.⁴⁷ are: 0 h (F1), 4.3 h (F2), 14.3 h (F3), 31.5 h (F4), 48.3 h (F5) and 59.3 h (F6).

density-stratified waters commonly occurs when the destabilizing effect of vertical gradients of horizontal velocity (shear, sh^2 ; see Methods) overcomes the stabilizing effect of the vertical density gradient (stratification, N^2). Shear instability and turbulence are predicted to develop for low, subcritical values of the gradient Richardson number, $Ri_g = N^2/sh^2 < 1/4$ (ref.²⁶). In our observational record, episodes of high near-surface ϵ (Fig. 1c) were associated with intensified winds on particular days (Fig. 1a), suggesting a physical driver of those turbulent patches. However, the occurrence of unstable conditions below 10 m did not exhibit a day-night cycle, as would be expected if shear instabilities generated the recurrent events of night-time dissipation. Instead, subcritical values of Ri_g within the water column became progressively rarer over the course of the experiment, as stratification increased (Fig. 1e). Unstable conditions were relatively frequent and widespread during

downwelling (I01), but retreated to the upper and bottom boundary layers during upwelling (I02 and I03). This disassociation between the observed turbulence and shear instabilities is succinctly illustrated by the weak correlation between ϵ and Ri_g (Spearman's $r = -0.14$, $P < 0.01$; Extended Data Fig. 3), which supports the notion that the night-time dissipation was sustained by a non-physical energy source.

A window onto the nature of such source is provided by the distribution of the volume backscattering strength (Sv), a metric of the occurrence of fish, recorded with a vessel-mounted echosounder: Sv was systematically enhanced at night (Fig. 1f), remarkably concurrent with elevated turbulent dissipation. The intensity of backscatter was highly correlated with ϵ for all the sampled backscattering frequencies (18–200 kHz, $r = 0.56$ –0.67, $P < 0.01$; Extended Data Fig. 3), suggesting that the night-time dissipation events were

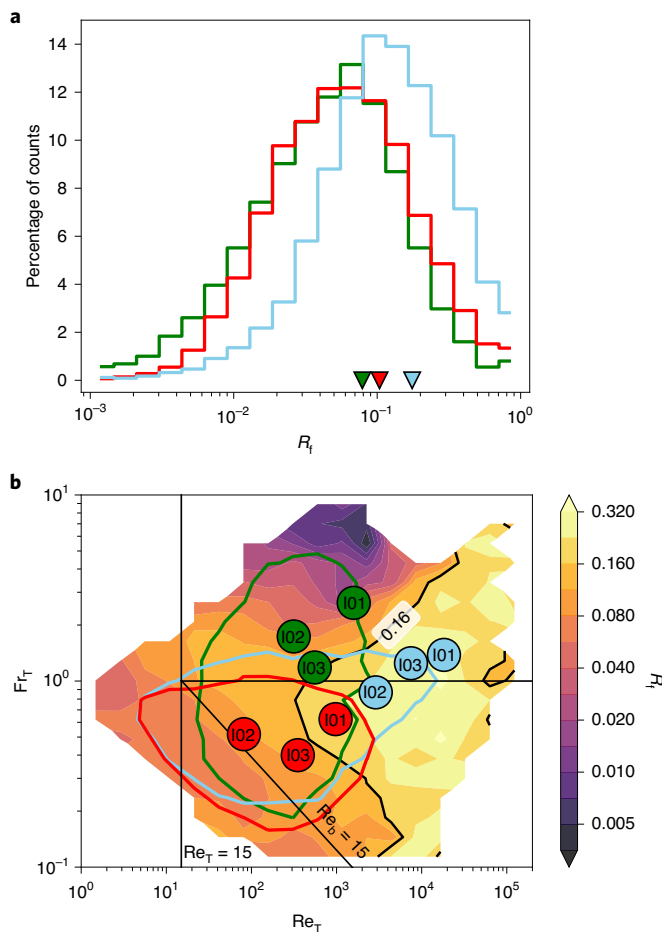


Fig. 3 | Mixing efficiency. **a**, Frequency distribution of R_f in the water column interior (10–25 m depth range) in periods dominated by biophysical turbulence (green) and periods dominated by geophysical turbulence (red), and in the near-surface layer (5–10 m) for the full time series (light blue). The mean values are indicated with triangles. **b**, Bin-averaged R_f in Re_T – Fr_T space. The high-efficiency $Fr_T=1$ (horizontal line), and molecular $Re_T=15$ (vertical) and $Re_b=15$ (oblique; $Re_b=(L_0/L_K)^{4/3}$) limits described by Ivey and Imberger³⁶ are shown as black lines. The mean values of Re_T and Fr_T are shown as circles for the three sampling periods (I01, I02 and I03) and for the different depth ranges. The green, red and light blue lines enclose bins in which the frequency of occurrence exceeds 0.5% of the total counts for periods of biophysical turbulence (green, 10–25 m), and interior (red, 10–25 m) and near-surface (light blue, 5–10 m) geophysical turbulence. The black contour represents the canonical value of $R_f=0.16$.

driven by fish aggregations. Consistent with this interpretation, high concentrations of European anchovy (*Engraulis encrasicolus*) eggs were detected in plankton net hauls that were performed every morning of the experiment and during the night of 8 July (Fig. 2). Local spawning of the eggs was indicated by both sets of hauls. In most of the morning hauls, the majority of eggs presented an F2 development stage (indicative of a time elapsed since spawning of 4–14 h), whereas the night-time haul (01:54 GMT, 03:54 local time) was dominated by freshly spawned eggs at stage F1 (corresponding to a time since spawning of <4 h). Note, however, that a lack of fish sampling gear on board prevented us from obtaining direct evidence of the presence of fish.

The picture that emerges from the net samples is one of a nocturnal aggregation of anchovies for spawning being responsible for driving our observed episodes of night-time dissipation. This view

is supported by the acoustic frequency response within the nocturnal turbulent patches, which was elevated at 18 kHz compared with higher frequencies (Extended Data Fig. 4), as previously described for anchovy aggregations²⁷. Previous reports of such aggregations inside the Rías of Northwest Iberia^{28,29}, which reveal spawning to occur between 19:00 and 6:00 GMT (peaking at midnight)³⁰, with a seasonal maximum in July–August³¹, also corroborate this. Thus, in the following, we will consider these episodes of intense nocturnal dissipation as being triggered by biophysical turbulence, and daytime periods of weaker dissipation as being dominated by geophysical turbulence.

Efficiency of turbulent mixing

As intense as the night-time biophysical turbulence may have been, did it induce commensurately substantial mixing? To address this question, we next characterized the mixing intensity by examining the record of temperature microstructure. This shows that the nocturnal biophysical turbulence events were associated with greater variance in the small-scale temperature gradients (Extended Data Fig. 5), and larger rates of thermal variance dissipation (χ , Extended Data Fig. 6a) and turbulent mixing of heat (quantified by the diffusivity K_T ; Fig. 1d). This mixing enhancement was most evident during I03 and I02, which exhibited more than tenfold increase in temperature-gradient variance above daytime levels over a broad wavenumber range (Extended Data Fig. 5), as well as an amplification of K_T by two orders of magnitude (relative to daytime values of $K_T < 10^{-6} \text{ m}^2 \text{s}^{-1}$; Fig. 1d). The mixing impact of biophysical turbulence was more muted during I01, when daytime turbulence was more energetic than during I02–I03 (Fig. 1d).

The mixing efficiency, defined here as the fraction of TKE converted to potential energy, was assessed for our entire dataset by computing the flux Richardson number, $R_f = K_T N^2 / (\epsilon + K_T N^2)$, where $K_T N^2$ and ϵ were respectively evaluated from microstructure measurements of the temperature gradient and shear. R_f varied by up to three orders of magnitude during our observational period, including episodes of both geophysical and biophysical turbulence (Fig. 3a and Extended Data Fig. 6). Averaged mixing efficiencies close to the canonical value of $R_f=0.16$ for geophysical, shear-driven turbulence were observed in the uppermost 10 m (mean $R_f=0.153$ (0.150–0.156 95% confidence intervals)), where turbulence was energized directly by wind. Below the surface (10–25 m), the frequency distribution of R_f was centred at lower values (mode $R_f \lesssim 0.1$), with broadly similar distributions for daytime geophysical turbulence and night-time biophysical turbulence (Fig. 3a). The R_f distribution for geophysical turbulence was slightly less negatively skewed, as values larger than the mode ($R_f \approx 0.1$) were more frequent than in the R_f distribution for biophysical turbulence. The average mixing efficiency during night-time biophysical turbulence events ($R_f=0.067$ (0.064–0.069)) was smaller than, but not substantially different to, the average value of R_f for background geophysical turbulence in the same depth interval ($R_f=0.088$ (0.086–0.090)). Our data thus demonstrate that, contrary to the common view at present²³, biophysical turbulence can act as a comparably efficient mixing agent to geophysical turbulence.

Discussion

Our observations reveal a consistent occurrence of elevated night-time levels of biophysical turbulence (reaching rates of dissipation as high as 10^{-6} – $10^{-5} \text{ W kg}^{-1}$, or two orders of magnitude above daytime values) during a two-week stretch, providing compelling evidence that fish can generate intense turbulence over prolonged periods. This contrasts with the results of several past investigations, which found biophysical turbulence challenging to detect in the field^{18,19,21}. There are, however, several threads of evidence to suggest that the representativeness of our results transcends the specific spatiotemporal context of our measurements. First, our

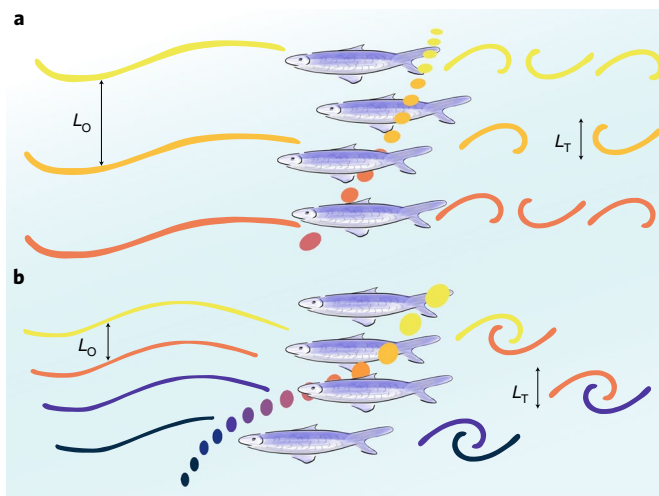


Fig. 4 | Schematic of the onset of efficient biomixing. **a,b**, Schematic representations of biophysical turbulence in contrasting levels of stratification, underpinning low (**a**) and elevated (**b**) mixing efficiency. **a**, Weak stratification (illustrated here by the coloured lines and dots depicting layers of different temperature) results in a large L_O compared with L_T . In this scenario, turbulent eddies are dissipated by viscosity before producing considerable mixing, and biophysical mixing is inefficient. Such conditions, mimicking those described by Visser⁸ for the main open-ocean pycnocline, are broadly captured by our observations during I01. **b**, In the second scenario, representing conditions during I02–I03, L_O shrinks as stratification increases, becoming comparable to the overturning scale. This situation allows the turbulent eddies to interact with the temperature/density profiles and transport heat/mass vertically before dissipating, thus leading to an increase in the efficiency of biomixing.

observed dissipation rates are similar to those documented previously in migrating zooplankton and krill layers^{17,32} and fish aggregations^{22,23,33}. They also conform to predictions by empirical models of biophysical turbulence that, on the basis of the size and characteristics of the swimming organisms^{13,19}, predict a rate of TKE production by the observed aggregations of $\sim 10^{-6} \text{ W kg}^{-1}$ (Methods). Finally, the aggregating fish behaviour that was responsible for the intense biophysical turbulence in our data is a recurrent feature in coastal upwelling areas in Northwest Iberia²⁸ and elsewhere³⁴. This is illustrated by measurements of acoustic backscatter acquired by a moored acoustic current profiler in our study area between 26 June and 19 July 2018, which revealed an enhancement of backscatter at almost every night in that extended period (Extended Data Fig. 7).

An important result of the present work pertains to the observation of intense biophysical turbulence with a mixing efficiency comparable to that of geophysical turbulence. This finding challenges expectations from several previous studies that pointed to a reduction in mixing efficiency, and in the rate of mixing itself, in association with biophysical turbulence^{22,23}. A theoretical explanation for such a reduction was provided by Visser⁸, who concluded that biophysical turbulence must necessarily be inefficient because the most abundant swimming organisms (zooplankton and fish) are small, and so produce small turbulent eddies (0.01–0.1 m). As these overturns would not be sufficiently large to interact with buoyancy forces, they would not induce mixing but would be rapidly destroyed by viscosity instead.

To unravel the discrepancy between Visser's argument and our results, we examined the relationship between the mixing efficiency (quantified by R_f) and a set of key turbulent parameters³⁵. This entailed projecting our data onto a space defined by the turbulent Reynolds (Re_T) and Froude (Fr_T) numbers³⁶ (Fig. 3b and Extended

Data Fig. 6). We approximated these two numbers using ratios of length scales that describe the competition between inertial, buoyancy and viscous forces in the fluid, following Ivey and Imberger³⁶. Although this simplified approach has some formal limitations³⁷, these do not affect the findings of our analysis (see discussion in the Methods). Re_T , computed here as $Re_T = (L_T/L_K)^{2/3}$, represents the ratio of the mean size of the energy-containing eddies (denoted by the Thorpe scale, L_T ; see Methods) to the viscosity-dominated Kolmogorov scale (L_K), and measures the competition between inertia and viscosity. Fr_T , here defined as $Fr_T = (L_O/L_T)^{2/3}$, quantifies the size of the observed turbulent eddies relative to the buoyancy or Ozmidov scale ($L_O = (\epsilon/N^3)^{1/2}$), at which turbulent eddies are strongly influenced by buoyancy³⁸. Thus, efficient mixing is expected when $L_T \approx L_O$ ($Fr_T \approx 1$), such that eddies interact with buoyancy forces and transport mass across the mean density gradient, and when Re_T is sufficiently large ($Re_T \gtrsim 100$), such that overturning motions are not readily damped by viscosity before they induce mixing³⁹. According to Visser⁸, biophysical turbulence is characterized by $Fr_T \gg 1$ (that is, $L_T \ll L_O$), such that $R_f \ll 0.16$.

Bin-averaging our observational estimates of R_f in Re_T – Fr_T space reveals that the mixing efficiency was maximal ($R_f \geq 0.16$) when $Re_T > 100$ –1,000 and $Fr_T \approx 1$ (Fig. 3b), as expected^{36,38}. These energetic conditions were only found in the surface layer (<10 m) that is directly energized by the wind. During the daytime, geophysical turbulence in the interior (10–25 m) was characterized by $Re_T < 100$ –1,000 and $Fr_T \approx 0.5$, which signal conditions under which turbulence is susceptible to suppression by buoyancy ($L_T > L_O$) and viscosity³⁹, such that the mixing efficiency might be curbed ($R_f \lesssim 0.1$). Night-time biophysical turbulence was more energetic ($Re_T \approx 1,000$), and contained overturns smaller than the Ozmidov scale ($L_T < L_O$, $Fr_T > 1$ –2). For the I01 sampling period, when relatively weak stratification ($N^2 \approx 2 \times 10^{-4} \text{ s}^{-2}$; Extended Data Table 1) and elevated ϵ resulted in enhanced $L_O \approx 1 \text{ m}$ and $Fr_T = 2.63$ (Extended Data Table 1), fish-induced eddies ($L_T \approx 10$ –20 cm, in line with the typical adult anchovy size in our study area⁴⁰ of ~12 cm) may have been too small to influence the background stratification, and the locus of the data in Re_T – Fr_T space suggests a reduction of R_f . In contrast, for I02 and I03, L_O was smaller (~20 cm) owing to a decrease in ϵ and a strengthening of stratification ($N^2 = 5$ – $10 \times 10^{-4} \text{ s}^{-2}$), and approached the size of the fish-driven turbulent overturns ($Fr_T \gtrsim 1$). Under these circumstances, the locus of the data in Re_T – Fr_T space indicated that $R_f \approx 0.1$; that is, in line with the mixing efficiency of geophysical turbulence. In summary, Visser's argument on the presumed inefficiency of biophysical turbulence does not hold in our observations because, contrary to their assumptions, L_O and L_T are comparable in a large portion of our dataset (Fig. 4).

Laboratory experiments suggest that the condition $L_O \approx L_T$, upon which efficient biomixing is contingent, is promoted by aggregations of swimmers, which can produce large, aggregation-scale turbulent eddies^{15,41}. Conversely, our observations suggest an alternative route towards efficient biomixing via an increase in stratification, which reduces buoyancy length scales (that is, L_O) to the point that they become comparable to turbulent eddy sizes, even if these are notably smaller than the aggregation scale. Our work thus shows that, besides biological factors—the agitated behaviour of the anchovies while spawning may have also played a role⁴¹—the mixing efficiency of biophysical turbulence is controlled by the background stratification, facilitating the injection of fish-induced TKE at the required scales. This conclusion implies that although biomixing might be inefficient within the main open-ocean pycnocline (where $L_O \approx 1 \text{ m}$)^{8,11}, it is likely to be considerably more effective in environments with stronger stratification, such as in seasonal pycnoclines or coastal seas (Fig. 4). Such a proposition seems particularly plausible in coastal regions, where riverine freshwater sources, solar heating and upwelling often give rise to highly stratified conditions⁴², and spawning aggregations of small pelagic fish (for example sardine,

herring or anchovy) are especially abundant^{34,40,43,44}. Hence, our results not only substantiate the prediction that fish aggregations can generate intense turbulent dissipation levels, comparable to storms¹³, but also show that elevated stratification fosters the occurrence of efficient biomixing. This highlights the potential of bio-physical turbulence to drive enhanced vertical exchanges in upper ocean areas with a rich biota, in which biomixing could contribute to the supply of nutrients⁴⁵ and the ventilation of deoxygenated waters⁴⁶, therefore promoting phytoplankton growth and reducing low-oxygen stress for higher trophic levels. The role of biomixing in shaping the physical and biogeochemical properties of productive upper ocean regions should thus be reassessed.

Online content

Any methods, additional references, Nature Research reporting summaries, source data, extended data, supplementary information, acknowledgements, peer review information; details of author contributions and competing interests; and statements of data and code availability are available at <https://doi.org/10.1038/s41561-022-00916-3>.

Received: 19 January 2021; Accepted: 24 February 2022;
Published online: 7 April 2022

References

- Thorpe, S. A. *The Turbulent Ocean* (Cambridge Univ. Press, 2005).
- Winters, K. B., Lombard, P. N., Riley, J. J. & D'Asaro, E. A. Available potential energy and mixing in density-stratified fluids. *J. Fluid Mech.* **289**, 115–128 (1995).
- Osborn, T. R. Estimates of the local rate of vertical diffusion from dissipation measurements. *J. Phys. Oceanogr.* **10**, 83–89 (1980).
- Oakey, N. S. Determination of the rate of dissipation of turbulent energy from simultaneous temperature and velocity shear microstructure measurements. *J. Phys. Ocean.* **12**, 256–271 (1982).
- Smyth, W. D. & Moum, J. N. Marginal instability and deep cycle turbulence in the eastern equatorial Pacific Ocean. *Geophys. Res. Lett.* **40**, 6181–6185 (2013).
- Gregg, M., D'Asaro, E., Riley, J. & Kunze, E. Mixing efficiency in the ocean. *Ann. Rev. Mar. Sci.* **10**, 443–473 (2017).
- Monismith, S. G., Koseff, J. R. & White, B. L. Mixing efficiency in the presence of stratification: when is it constant? *Geophys. Res. Lett.* **45**, 5627–5634 (2018).
- Visser, A. W. Biomixing of the oceans? *Science* **316**, 838–839 (2007).
- Wunsch, C. & Ferrari, R. Vertical mixing, energy, and the general circulation of the oceans. *Annu. Rev. Fluid Mech.* **36**, 281–314 (2004).
- Munk, W. H. Abyssal recipes. *Deep Sea Res.* **13**, 707–730 (1966).
- Kunze, E. Biologically generated mixing in the ocean. *Ann. Rev. Mar. Sci.* **11**, 215–226 (2019).
- Katija, K. Biogenic inputs to ocean mixing. *J. Exp. Biol.* **215**, 1040–1049 (2012).
- Huntley, M. E. & Zhou, M. Influence of animals on turbulence in the sea. *Mar. Ecol. Prog. Ser.* **273**, 65–79 (2004).
- Dewar, W. K. et al. Does the marine biosphere mix the ocean? *J. Mar. Res.* **64**, 541–561 (2006).
- Houghton, I. A., Koseff, J. R., Monismith, S. G. & Dabiri, J. O. Vertically migrating swimmers generate aggregation-scale eddies in a stratified column. *Nature* **556**, 497–500 (2018).
- Farmer, D. D., Crawford, G. B. & Osborn, T. R. Temperature and velocity microstructure caused by swimming fish. *Limnol. Oceanogr.* **32**, 978–983 (1987).
- Kunze, E., Dower, J. F., Bevaridge, I., Bawey, R. & Bartlett, K. P. Observations of biologically generated turbulence in a coastal inlet. *Science* **313**, 1768–1770 (2006).
- Rousseau, S., Kunze, E., Dewey, R., Bartlett, K. & Dower, J. On turbulence production by swimming marine organisms in the open ocean and coastal waters. *J. Phys. Oceanogr.* **40**, 2107–2121 (2010).
- Lorke, A. & Probst, W. N. In situ measurements of turbulence in fish shoals. *Limnol. Oceanogr.* **55**, 354–364 (2010).
- Sato, M., Klymak, J. M., Kunze, E., Dewey, R. & Dower, J. F. Turbulence and internal waves in Patricia Bay, Saanich Inlet, British Columbia. *Cont. Shelf Res.* **85**, 153–167 (2014).
- Simoncelli, S., Thackeray, S. J. & Wain, D. J. On biogenic turbulence production and mixing from vertically migrating zooplankton in lakes. *Aquat. Sci.* **80**, 35 (2018).
- Gregg, M. C. & Horne, J. K. Turbulence, acoustic backscatter, and pelagic nekton in Monterey Bay. *J. Phys. Oceanogr.* **39**, 1097–1114 (2009).
- Pujana, K., Moum, J. N., Smyth, W. D. & Warner, S. J. Distinguishing ichthyogenic turbulence from geophysical turbulence. *J. Geophys. Res. Oceans* **120**, 3792–3804 (2015).
- Álvarez-Salgado, X., Gago, J., Míguez, B., Gilcoto, M. & Pérez, F. Surface waters of the NW Iberian Margin: upwelling on the shelf versus outwelling of upwelled waters from the Rias Baixas. *Estuar. Coast. Shelf Sci.* **51**, 821–837 (2000).
- Pardo, P. C., Gilcoto, M. & Pérez, F. F. Short-time scale coupling between thermohaline and meteorological forcing in the Ría de Pontevedra. *Sci. Mar.* **65**, 229240 (2001).
- Miles, J. Richardson's criterion for the stability of stratified shear flow. *Phys. Fluids* **29**, 3470 (1986).
- Park, J. et al. Frequency responses of anchovy schools in the South Sea of South Korea in spring and winter. *J. Korean Soc. Fish. Technol.* **52**, 111–120 (2016).
- Ferreiro, M. J. *El Ictioplancton de la Ría de Vigo*. PhD thesis, Univ. Santiago de Compostela (1985).
- Motos, L., Uriarte, A. & Valencia, V. The spawning environment of the Bay of Biscay anchovy (*Engraulis encrasicolus* L.). *Sci. Mar.* **60**, 117–140 (1996).
- Motos, L. Reproductive biology and fecundity of the Bay of Biscay anchovy population (*Engraulis encrasicolus* L.). *Sci. Mar.* **60**, 195–207 (1996).
- Sola, A., Motos, L., Franco, C. & Lago de Lanzos, A. Seasonal occurrence of pelagic fish eggs and larvae in the Cantabrian Sea (VIIc) and Galicia (IXa) from 1987 to 1989. In: *ICES Conference and Meeting Documents 1990* H:25 (1990).
- Simpson, J. H. et al. The annual cycle of energy input, modal excitation and physical plus biogenic turbulent dissipation in a temperate lake. *Water Resour. Res.* **57**, e2020WR029441 (2021).
- Hooper, J. A., Baringer, M. O., St. Laurent, L. C., Dewar, W. K. & Nowacek, D. Dissipation processes in the Tongue of the Ocean. *J. Geophys. Res. Oceans* **121**, 3159–3170 (2016).
- Claramunt, G., Cubillos, L., Herrera, G. & Díaz, E. Spawning marker patterns of *Engraulis ringens* of northern Chile. *Fish. Res.* **219**, 105306 (2019).
- Caulfield, C. Layering, instabilities, and mixing in turbulent stratified flows. *Annu. Rev. Fluid Mech.* **53**, 113–145 (2021).
- Ivey, G. N. & Imberger, J. On the nature of turbulence in a stratified fluid. Part I: the energetics of mixing. *J. Phys. Oceanogr.* **21**, 650–658 (1991).
- Mater, B. D., Schaad, S. M. & Venayagamoorthy, S. K. Relevance of the Thorpe length scale in stably stratified turbulence. *Phys. Fluids* **25**, 076604 (2013).
- Mashayek, A. et al. Efficiency of turbulent mixing in the abyssal ocean circulation. *Geophys. Res. Lett.* **44**, 6296–6306 (2017).
- Gargett, A. E., Osborn, T. R. & Nasmyth, P. W. Local isotropy and the decay of turbulence in a stratified fluid. *J. Fluid Mech.* **144**, 231–280 (1984).
- Massé, J., Uriarte, A., Angélico, M. M. & Carrera, P. *Pelagic Survey Series for Sardine and Anchovy in ICES Subareas 8 and 9 (WGACCEGG)—Towards an Ecosystem Approach* Cooperative Research Report No. 332 (ICES, 2018).
- Tanaka, M., Nagai, T., Okada, T. & Yamazaki, H. Measurement of sardine-generated turbulence in a large tank. *Mar. Ecol. Prog. Ser.* **571**, 207–220 (2017).
- Largier, J. L. Upwelling bays: how coastal upwelling controls circulation, habitat, and productivity in bays. *Ann. Rev. Mar. Sci.* **12**, 415–447 (2020).
- Cury, P. et al. Small pelagics in upwelling systems: patterns of interaction and structural changes in 'wasp-waist' ecosystems. *ICES J. Mar. Sci.* **57**, 603–618 (2000).
- Huse, G. A spatial approach to understanding herring population dynamics. *Can. J. Fish. Aquat. Sci.* **73**, 177–188 (2016).
- Sharples, J. et al. Phytoplankton distribution and survival in the thermocline. *Limnol. Oceanogr.* **46**, 486–496 (2001).
- Diaz, R. J. Overview of hypoxia around the world. *J. Environ. Qual.* **30**, 275–281 (2001).
- Ibaibarriaga, L. et al. Characterization of stage-classified biological processes using multinomial models: a case study of anchovy (*Engraulis encrasicolus*) eggs in the Bay of Biscay. *Can. J. Fish. Aquat. Sci.* **64**, 539–553 (2007).

Publisher's note Springer Nature remains neutral with regard to jurisdictional claims in published maps and institutional affiliations.

© The Author(s), under exclusive licence to Springer Nature Limited 2022

Methods

Sampling overview. The REMEDIOS sampling campaign was carried out off the Galician coast (Northwest Iberian Peninsula) between 29 June and 18 July 2018 on board RV *Ramón Margalef* (Extended Data Fig. 1). Three intensive sampling time series were performed: I01 (08:00 on 2 July 2018 am to 08:40 on 6 July 2018), I02 (22:07 on 7 July 2018 to 05:23 on 9 July 2018) and I03 (17:50 on 10 July 2018 to 19:30 on 14 July 2018) at station P2-Bueu, inside the Ría de Pontevedra (42.357°N, 8.773°W, mean depth 30 m). During these sampling periods, five casts were performed every 30 min with a microstructure profiler⁴⁸, resulting in a total of 1,658 profiles (~50 km of microstructure data). This sequence was interrupted every 6 h for water collection with a Rosette. Water velocity profiles were continuously recorded with a bottom-moored acoustic Doppler current profiler, and the volume backscattering strength was registered with a hull-mounted echosounder.

Microstructure measurements. The microstructure profiler was equipped with two shear microstructure sensors (type PNS06) and a temperature microstructure sensor (type FP07), complemented with a high-accuracy conductivity–temperature–depth (CTD) and an accelerometer to assess the instrument's vibration. The various channels were sampled at 1,024 Hz, and the instrument was loosely tethered and operated in free-falling mode at a nominal vertical speed of 0.6–0.7 m s⁻¹. ε and χ were calculated by integrating the vertical shear and vertical temperature-gradient spectra over half-overlapping segments of 2 m. The shear microstructure signal was de-noised for instrument vibration using the accelerometer signal⁴⁹. A pseudo-shear signal was also derived from the accelerometer to assess ε contamination by instrument vibration. The temperature-gradient spectra were corrected for the FP07 time response ($\tau = 12$ m s⁻¹) with a double-pole function before integration⁵⁰. The shear spectra were integrated from a minimum wavenumber of two cycles per metre (cpm). The upper integration limit was estimated iteratively from an initial guess of 14 cpm until convergence with the Kolmogorov wavenumber ($k_c = \frac{1}{2\pi}(\varepsilon\nu^{-3})^{1/4}$) was achieved. The upper cutoff was set to a maximum value of 30 cpm to avoid the spectral region where the spatial response of the shear probe becomes limiting and noise is introduced by instrument vibrations. The temperature-gradient spectra were also integrated from 2 cpm. The upper integration limit in this case was chosen as the minimum of the following wavenumbers: (1) the wavenumber at which the measured spectrum has an amplitude smaller than double the amplitude of the empirical noise spectrum (see Extended Data Fig. 5 and Supplementary Figs. 1 and 2); (2) the wavenumber at which the time response correction is larger than a factor of 100; and (3) the wavenumber corresponding to a frequency of 60 Hz. The missing variance at wavenumbers beyond the integration limits was estimated by assuming that the shear and temperature spectra, respectively, follow the empirical Nasmyth and Bachelor forms⁵¹. Before the missing-variance correction, ε values were corrected for the probe's spatial response using the polynomial factors given by the manufacturer. Note that the variance correction can be substantial for high levels of dissipation (that is, $\varepsilon > 10^{-6}$ W kg⁻¹); however, the measured spectra show excellent agreement with the empirical universal forms for intense turbulence over the resolved wavenumber range (Supplementary Fig. 1), supporting the robustness of the estimation. This methodology is described in more detail elsewhere⁵². During night-time biomixing periods, fish impacts on the profiler were often apparent in the shear and pseudo-shear (accelerometer) records (Supplementary Fig. 2). These data segments were manually identified and excluded from further analysis. Impacts were frequent during I01 (1,772 of 2,829 segments discarded), but rare during I02 (129 of 1,866 segments discarded) and I03 (114 of 3,378 segments discarded) (Extended Data Table 1).

Mixing characterization. The stability with respect to shear-driven turbulence was characterized with the gradient Richardson number, $Ri_g = N^2/sh^2$, where $N^2 = -g/\rho(\partial_z\rho)$ is the buoyancy frequency, ρ is the potential density and $sh^2 = (\partial_z u)^2 + (\partial_z v)^2$ is the squared vertical shear, with u and v the zonal and meridional velocity components. In these equations, ∂_z represents a vertical derivative. The turbulent diffusivity for heat was calculated using the Osborn–Cox⁵³ relation as $K_T = 0.5\chi/(\partial_z T)^2$, where $\partial_z T$ is the background temperature gradient. The mixing efficiency was quantified with the flux Richardson number ($R_f = K_T N^2/(\varepsilon + K_T N^2)$), and the vertical size of turbulent overturns with the Thorpe length scale (L_T). L_T was computed by comparing the measured potential density with an adiabatically resorted density profile⁵⁴. Other relevant scales for turbulence are the Ozmidov ($L_O = (\varepsilon N^{-3})^{1/2}$) and the Kolmogorov ($L_K = (\nu^3 \varepsilon^{-1})^{1/4}$) length scales, where ν is the kinematic viscosity, $\sim 10^{-6}$ m² s⁻¹.

Acoustic backscatter and fish density. A Simrad EK80 echosounder operated split-beam transducers of 18, 38, 70, 120 and 200 kHz in continuous-wave mode with the maximum pinging rate, registering 50 m of data in the vertical direction. The pulse duration was set to 1 ms for all frequencies, while the beam width was 11° for 18 kHz and 7° for higher frequencies. The transmitting power was 1,600, 1,600, 675, 225 and 135 W, respectively, for each frequency. The standard sphere calibration procedure was performed after the survey⁵⁵. A depth- and time-averaged volume backscattering coefficient (Sv, dB relative to 1 m² m⁻³, dB hereafter) was produced by computing arithmetic means in the linear domain in

bins of 2 m by 30 min. Prior to averaging, we removed the first 6 m of data, where ringing noise (remaining transducer vibration while already in listening mode) affected the 18 kHz echogram.

European anchovy eggs. The sampling of *Engraulis encrasicolus* eggs was performed by means of oblique hauls from the surface down to 3 m above the bottom (~30 m depth) with a double-WP2 plankton net (HydroBios; 3.95 m² mouth area; 200 µm mesh size) at a descending (ascending) rate of 50 (30) m min⁻¹ and a trawling speed of 2 knot. Each net carried a mechanical flowmeter (General Oceanics) to estimate the volume of sampled water (between approximately 17 and 32 m³). The collected samples were preserved with buffered formaldehyde (4% final concentration). Counting and definition of the development state of eggs were carried out with a stereoscopic binocular (Nikon SMZ-10). Sample aliquots of 20 ml, from a solution of 400 ml of the whole sample, were used for those purposes. To illustrate development state (Extended Data Table 2), microphotographs were taken with a stereoscopic binocular and dedicated image acquisition software (Nikon SMZ-1270 and NIS-Elements). The development state was classified in stages according to morphological properties of the embryos⁵⁶. The eggs collected during the survey were classified into six stages (F1 to F6), focusing on the characterization of development in the first 12 h after spawning and considering a reference temperature of 17°C (ref. ⁴⁷). Stages applied here (F1 to F6), their equivalence to the stages ('staging') proposed in ref. ⁵⁶ (I to XI), stage duration after spawning in hours (for an ambient temperature of 17°C) and morphological characteristics of the embryos (from table A1.3 of ref. ⁴⁰) are given in Extended Data Table 2.

Currents and continuous backscatter. An RD Instruments acoustic Doppler current profiler (300 kHz) was bottom-moored looking upwards at station P2-Bueu before the start of the cruise (26 June 2018), and was recovered after the end of the cruise (19 July 2018) by RV *Kraken*. The three-dimensional current was recorded every 5 min as the average of 120 individual pings in 70 layers of 0.5 m spanning the water column from 4 m above the bottom to the surface. The acoustic Doppler current profiler backscatter was converted to volume backscattering strength (Sv, in dB) following the procedure used in refs. ^{57,58}.

TKE production by anchovy aggregations. TKE production by the anchovy aggregations was estimated as $P_{TKE} = 0.072/3 N^{1/5} L^{1/5} \nu^{0.2} \approx 10^{-6}$ W kg⁻¹, following refs. ^{13,19}, where $\nu \approx 1 \times 10^{-6}$ m² s⁻¹ is the molecular viscosity of seawater. A characteristic fish size of $L = 12$ cm (corresponding to the modal size of 1-yr-old anchovy adults⁴⁰) and a swimming speed of $U \approx 36$ cm s⁻¹ (equivalent to three body lengths per second⁵⁹) were used in the calculation. The fish concentration in the aggregations (n , individuals per m³) was calculated using the relationship between the target strength for a given species (TS) and the observed volume backscattering (Sv = TS + 10 log₁₀(n)). Using the TS at 38 kHz employed for the PELACUS surveys in this area⁴⁰ (TS = 20 × log₁₀(L) – 72.6 = –51.02), the recorded mean Sv in the shoal at 38 kHz (–53.63 dB for I02) would convert into a concentration of $n = 0.5$ individuals per m³.

Mixing efficiency in the Re_T – Fr_T diagram. To synthesize the variability of R_f (a measure of the mixing efficiency) in our cruise measurements, and rationalize the relatively high efficiency diagnosed for biophysical mixing, we placed our data in a Reynolds–Froude (Re_T – Fr_T) numbers diagram. Projection onto Re_T – Fr_T space is useful to describe the balance of forces in a turbulent fluid, which, in turn, underpins the efficiency of mixing. The state-of-the-art profiling instruments enabling quantification of turbulence in natural waters, such as the microstructure profiler employed in this study, do not directly measure Re_T and Fr_T . Thus, following common practice in ocean turbulence works⁵⁶, we approximated these quantities using turbulence length scales that can be directly assessed from the measurements (L_O and L_T), such that:

$$Re_T = \left(\frac{L_T}{L_K} \right)^{4/3} \quad (1)$$

and

$$Fr_T = \left(\frac{L_O}{L_T} \right)^{2/3}. \quad (2)$$

Recent evidence from direct numerical simulations³⁷ suggests that these approximate definitions of Re_T and Fr_T are only valid in a weakly stratified regime, defined by $L_T < L_O$. According to these authors, the length scale dependencies of Re_T and Fr_T differ for a highly stratified regime ($L_T > L_O$), which would apply to a substantial portion of our data. In such a regime,

$$Re_T = \left(\frac{L_T^3}{L_O^2 L_K} \right)^{4/3} \quad (3)$$

and

$$Fr_T = \left(\frac{L_O}{L_T} \right)^2. \quad (4)$$

We assessed the impact that this regime shift had for our conclusions by recalculating Re_T and Fr_T using equations (3) and (4). The results (Supplementary Fig. 3) show that the diagram is ‘stretched’ relative to Fig. 3b, owing to the stronger power dependencies of the scaling functions in the highly stratified regime. However, the key patterns supporting our findings remain unchanged.

Specifically, biophysical turbulence (green contour) spans a wide range of Fr_T values, with some data points intruding into an area with $Fr_T > 1$ and a very low mixing efficiency, but with many others located closer to $Fr_T = 1$ (and even $Fr_T < 1$), where the mixing efficiency is higher. In contrast, interior geophysical turbulence (red contours) appear in an area with $Fr_T < 1$ and possible turbulence suppression by buoyancy forces (around the oblique line representing $Re_T \approx 10$, where buoyancy forces suppress mixing). Geophysical turbulence in the wind-influenced surface layer displays data points in an energetic region of higher efficiency. In summary, although the shape of the diagram is slightly different, our key conclusions—that biomixing is occasionally suppressed because $Fr_T > 1$ (particularly during I01), but not as strong stratification reduces Fr_T during I02–I03; and that geophysical turbulence in the interior is partly suppressed by buoyancy, thereby making the efficiency of biophysical and geophysical mixing comparable—hold, irrespective of the approach chosen to estimate the turbulence parameters.

Data availability

The data that support the findings of this study are available via Zenodo at <https://doi.org/10.5281/zenodo.5559023>.

Code availability

The scripts used for microstructure data processing are freely available via GitHub at https://github.com/bieitofernandez/MSS_processing.

References

48. Prandke, H. & Stips, A. Test measurements with an operational microstructure-turbulence profiler: detection limit of dissipation rates. *Aquat. Sci.* **60**, 191–209 (1998).
49. Levine, E. R. & Lueck, R. G. Turbulence measurement from an autonomous underwater vehicle. *J. Atmos. Ocean. Technol.* **16**, 1533–1544 (1999).
50. Gregg, M. C. Uncertainties and limitations in measuring ϵ and $\chi(T)$. *J. Atmos. Ocean. Technol.* **16**, 1483–1490 (1999).
51. Batchelor, G. K., Howells, I. D. & Townsend, A. A. Small-scale variation of convected quantities like temperature in turbulent fluid: part 1. General discussion and the case of small conductivity. *J. Fluid Mech.* **5**, 113–133 (1959).
52. Piccolroaz, S., Fernández-Castro, B., Toffolon, M. & Dijkstra, H. A. A multi-site, year-round turbulence microstructure atlas for the deep perialpine Lake Garda. *Sci. Data* **8**, 188 (2021).
53. Osborn, T. R. & Cox, C. S. Oceanic fine structure. *Geophys. Fluid Dynam.* **3**, 321–345 (1972).
54. Thorpe, S. A. Turbulence and mixing in a Scottish Loch. *Phil. Trans. R. Soc. Lond. A* **286**, 125–181 (1977).
55. Demer, D. A. et al. *Calibration of Acoustic Instruments Cooperative Research Report No. 326* (ICES, 2015).
56. Moser, M. H. & Ahlstrom, E. H. in *An Egg Production Method for Estimating Spawning Biomass of Pelagic Fish: Application to the Northern Anchovy, Engraulis mordax*. NOAA Technical Report No. NMFS 36, 37–42 (US Department of Commerce, 1985).
57. Deines, K. L. Backscatter estimation using broadband acoustic Doppler current profilers. In *Proc. IEEE Sixth Working Conference on Current Measurement* 249–253 (IEEE, 1999); <https://doi.org/10.1109/CCM.1999.755249>
58. Mullison, J. *Backscatter Estimation Using Broadband Acoustic Doppler Current Profilers—Updated Application Note FSA-031* (Teledyne RD Instruments, 2017).
59. Peraltilla, S. & Bertrand, S. In situ measurements of the speed of Peruvian anchovy schools. *Fish. Res.* **149**, 92–94 (2014).

Acknowledgements

Funding for this work was provided by the Spanish Ministry of Economy and Innovation under the research project REMEDIOS (grant number CTM2016-75451-C2-1-R) to B.M.-C. B.F.C. was supported by the Spanish Ministry of Economy and Innovation through a Juan de La Cierva-Formación postdoctoral fellowship (grant number FJCI-641 2015-25712) and by the European Union’s Horizon 2020 research and innovation programme under the Marie Skłodowska-Curie grant agreement number 834330 (SO-CUP). E.B. was supported by a postgraduate fellowship (grant number ED481A-2019/288) from Xunta de Galicia, co-funded by FSE Galicia. A.C. was supported by a postgraduate fellowship FPI (grant number BES-2017-080935) from the Spanish Ministry of Economy and Competitiveness. A.C.N.G. acknowledges the support of the Royal Society and the Wolfson Foundation. We thank all the participants in the REMEDIOS cruise, particularly the crew of the RV *Ramón Margalef* for their support, and P. Rial, I. Ramilo and M. Villamáñan for their contribution to data collection. We are also thankful to G. Casas for his assistance in counting and staging anchovy eggs. We are especially grateful to P. Choucifor her logistical support during the cruise and assistance with microstructure data processing. S. Piccolroaz and Ó. Sepúlveda Steiner contributed to the development of the microstructure processing functions. C. Ofelio designed the illustration in Fig. 4.

Author contributions

B.F.C. and B.M.-C. conceived the study. B.M.-C. led the cruise. B.F.C., E.N., M.G., E.B., A.C. and B.M.-C. participated in the data collection. B.F.C., M.P., E.N. and M.G. analysed the data. All the authors contributed to the scientific discussions and interpretation of the results. B.F.C., B.M.-C. and A.C.N.G. wrote the manuscript with contributions from all the co-authors.

Competing interests

The authors declare no competing interests.

Additional information

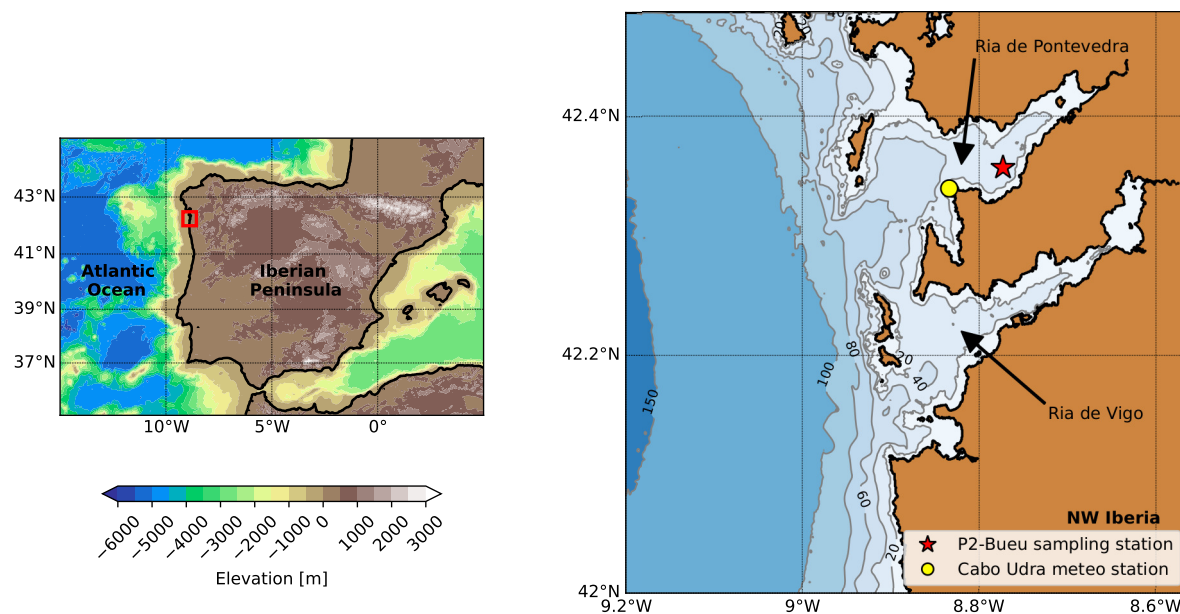
Extended data is available for this paper at <https://doi.org/10.1038/s41561-022-00916-3>.

Supplementary information The online version contains supplementary material available at <https://doi.org/10.1038/s41561-022-00916-3>.

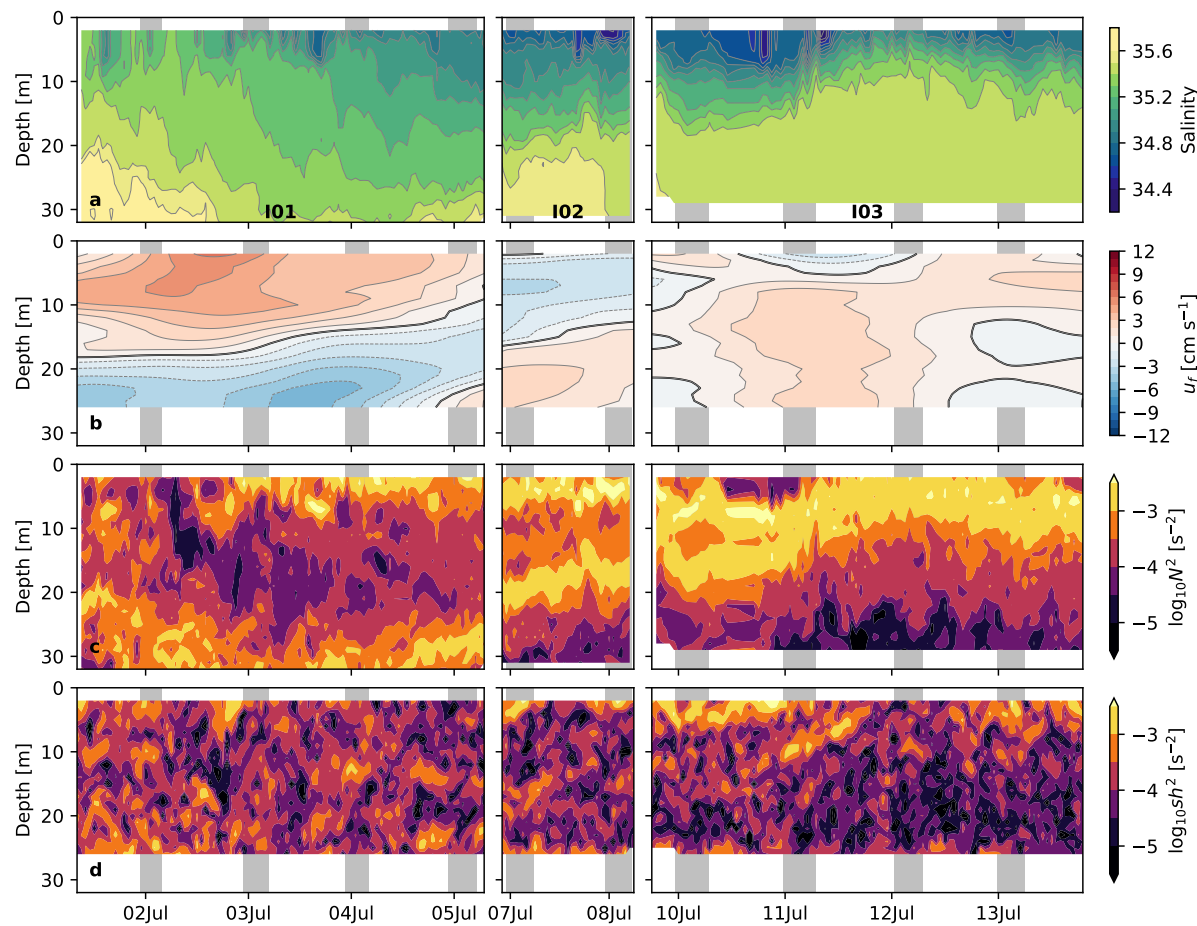
Correspondence and requests for materials should be addressed to Bieito Fernández Castro.

Peer review information *Nature Geoscience* thanks Jonathan Nash, Hidekatsu Yamazaki and the other, anonymous, reviewer(s) for their contribution to the peer review of this work. Primary Handling Editors: Simon Harold, Kyle Frischkorn and James Super, in collaboration with the *Nature Geoscience* team.

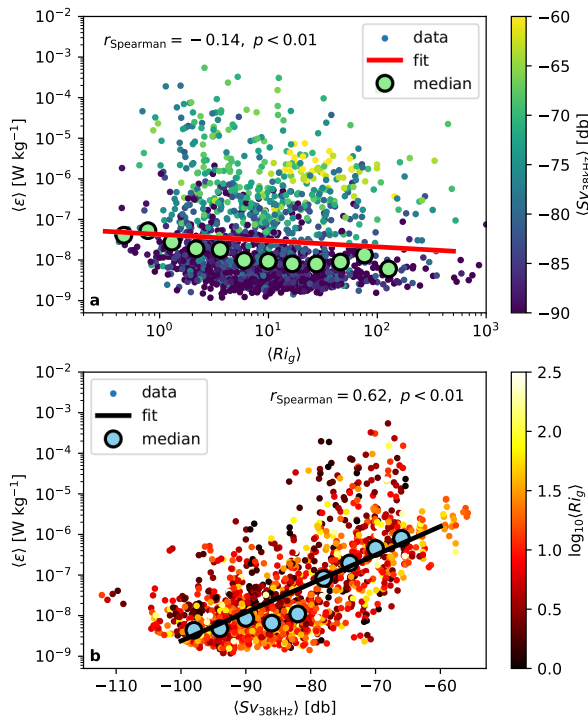
Reprints and permissions information is available at www.nature.com/reprints.



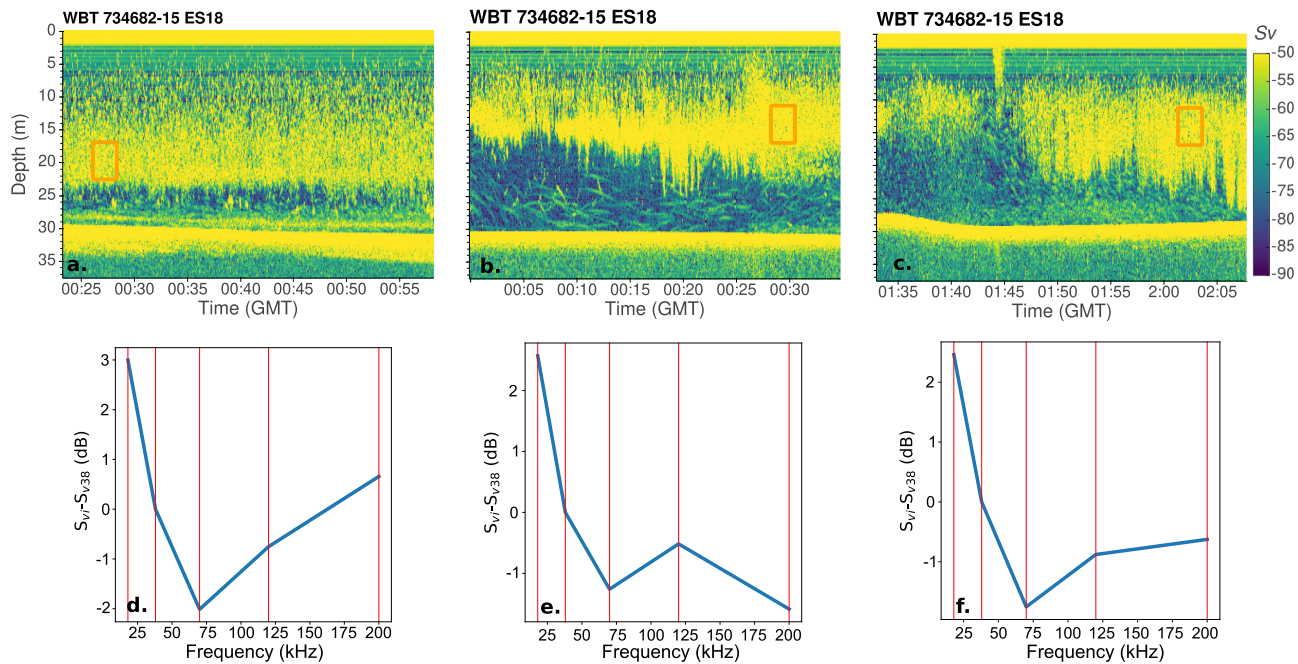
Extended Data Fig. 1 | Location of survey. Map of the location of the REMEDIOS sampling station P2-Bueu (red star, 42.357°N, 8.773°W, mean depth 30 m) in the Ría de Pontevedra (off the Galician coast, NW Iberian Peninsula). The location of the closest Meteogalicia (www.meteogalicia.gal) meteorological station (yellow dot, Cape Udra, 42.340°N, -8.884°E) is also shown.



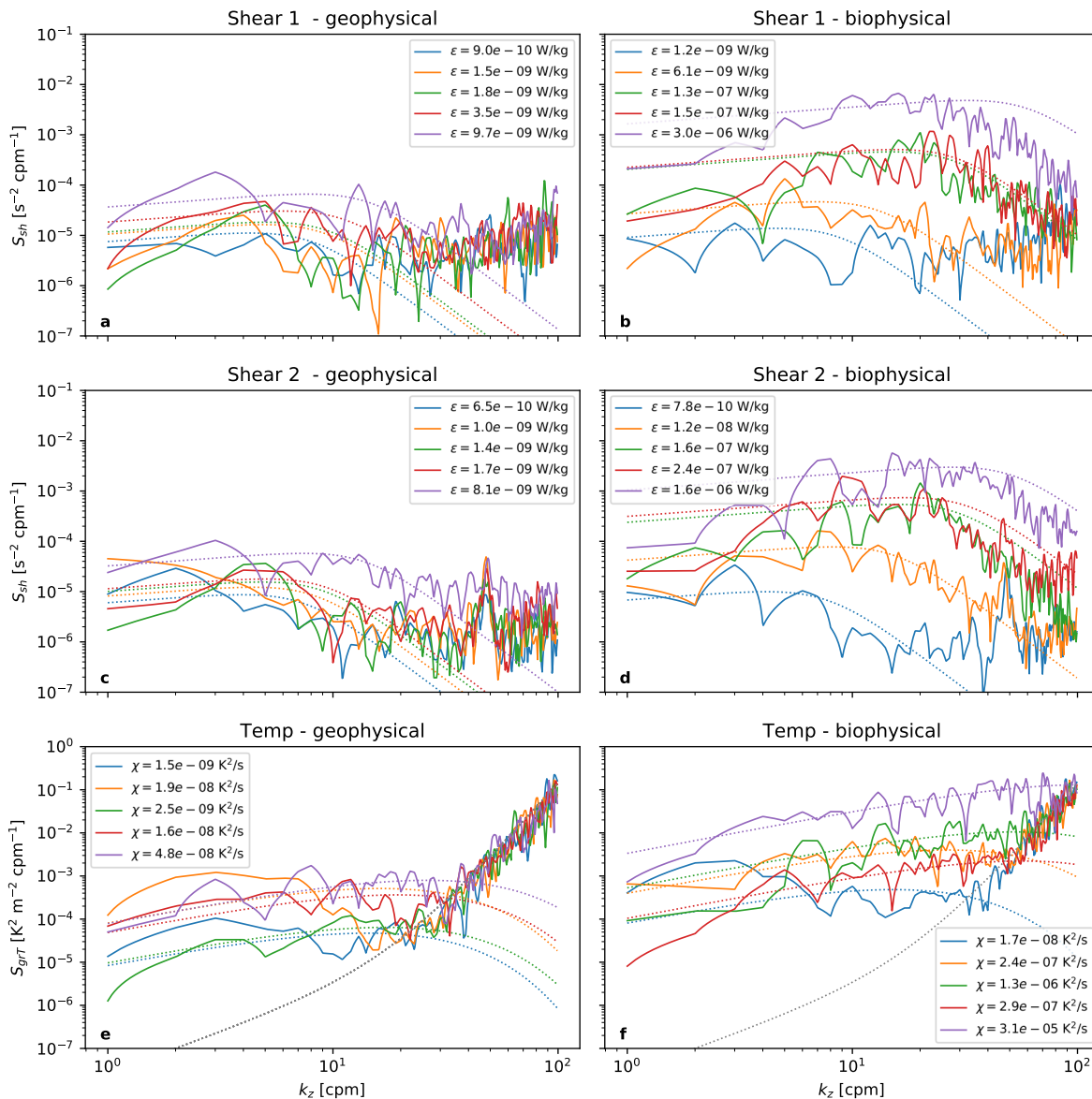
Extended Data Fig. 2 | Hydrographic setting. Hourly mean time series of **a** salinity, **b** de-tided eastward velocity (u_e), **c** squared buoyancy frequency (N^2), and **d** squared vertical shear of horizontal velocity (sh^2) during the three sampling periods (I01, I02 and I03). Gray shading indicates night-time periods of enhanced biophysical turbulence. These periods were determined by inspection of the turbulent dissipation rate and volume backscattering strength records. De-tided residual velocity was calculated with a 24/25/24 h Godin filter. Positive eastward velocity imports offshore waters into the Ría, and negative westward velocity exports onshore waters out of the Ría. Note the use of logarithmic color scale in panels **c** and **d**.



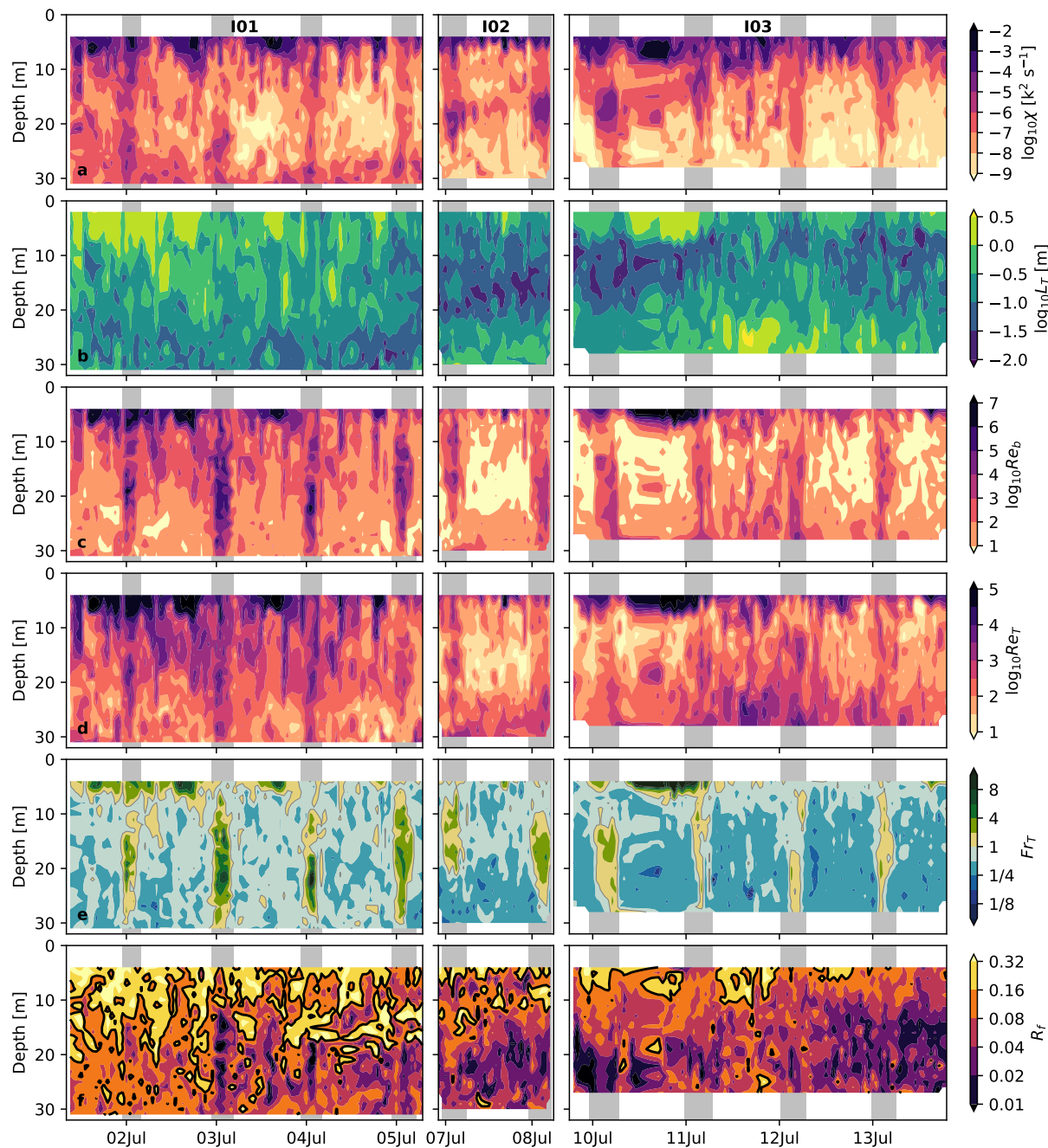
Extended Data Fig. 3 | Sources of turbulence. Depth-averaged (10–25 m) ε vs. **a** depth-averaged R_i and **b** 38 KHz volume backscattering strength (Sv). ε median values in bins of R_i and $Sv_{38\text{kHz}}$ are indicated as larger circles. Linear fits in logarithmic scale and Spearman correlation coefficients are shown. The dot color scale represents $Sv_{38\text{kHz}}$ and R_i in panels **a** and **b**, respectively.



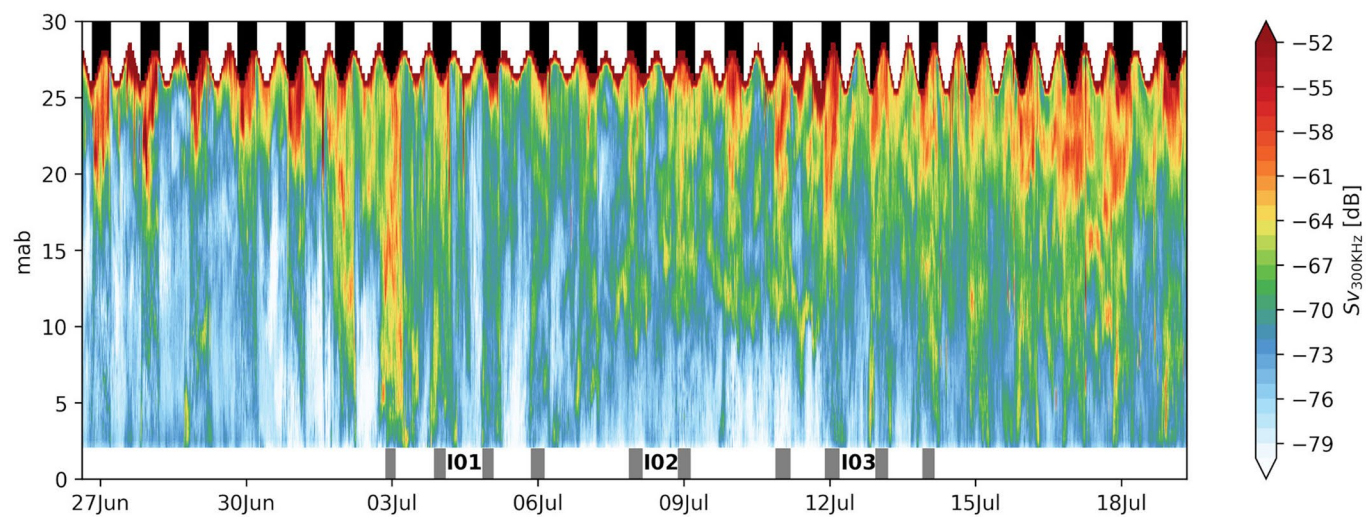
Extended Data Fig. 4 | Acoustic backscatter frequency response. Three examples of night-time echograms at 18 kHz, recorded during sampling periods I01 (a, 4 July), I02 (b, 8 July) and I03 (c, 12 July). Panels d-f show the mean frequency response (Sv at each frequency minus Sv at 38 kHz) for the region enclosed by the orange rectangles in panels a-c.



Extended Data Fig. 5 | Microstructure spectra. Randomly selected wavenumber (k_z , units: cycles per meter, cpm) spectra of vertical shear (a-d) and temperature gradient (e,f) microstructure between 10 and 25 m depth, during the third sampling period (I03). Periods dominated by geophysical turbulence are shown in the left column, and those dominated by biophysical turbulence (gray shading in Figure 1), in the right column. The corresponding universal spectra are indicated by dotted colored lines, and the computed dissipation rates of turbulent kinetic energy (ε) and thermal variance (χ) are reported. Spectra recorded with the two shear sensors over the same portion of the water column are shown a, b and c, d, respectively. Empirical spectra of thermistor noise are represented by the gray dotted line e,f.



Extended Data Fig. 6 | Turbulence and mixing parameters. Time series of hourly mean **a** rate of dissipation of thermal variance (χ), **b** Thorpe scale (L_T), **c** buoyancy Reynolds number (Re_b), **d** turbulent Reynolds number (Re_T), **e** turbulent Froude number (Fr_T), and **f** flux Richardson number (R_f , a proxy for mixing efficiency) during the three sampling periods (I01, I02 and I03). Gray shading indicates night-time periods of enhanced biophysical turbulence. Note the use of a logarithmic color scale in all panels.



Extended Data Fig. 7 | ADCP backscatter. Time series of volume backscattering strength (S_v , dB) measured with a 300 kHz bottom-moored ADCP. Nights and biomixing events during the sampling periods (I01, I02 and I03) are indicated with black and gray shading, respectively. The y-axis coordinate is meters above bottom (mab).

Extended Data Table 1 | Mean turbulent properties

	I01		I02		I03	
	Geophysical	Biophysical	Geophysical	Biophysical	Geophysical	Biophysical
n_{good} (n_{impacts})	8517 (0)	1772 (1057)	2573 (0)	1737 (129)	7531 (0)	3264 (114)
N^2 [s $^{-2}$]	$2.15 [2.10 - 2.21] \times 10^{-4}$	$2.00 [1.93 - 2.1] \times 10^{-4}$	$7.73 [7.44 - 8.07] \times 10^{-4}$	$7.79 [7.37 - 8.11] \times 10^{-4}$	$4.59 [4.45 - 4.72] \times 10^{-4}$	$5.11 [4.92 - 5.32] \times 10^{-4}$
sh^2 [s $^{-2}$]	$2.22 [2.16 - 2.28] \times 10^{-4}$	$2.47 [2.38 - 2.59] \times 10^{-4}$	$1.85 [1.47 - 1.67] \times 10^{-4}$	$1.68 [1.58 - 1.78] \times 10^{-4}$	$1.30 [1.24 - 1.38] \times 10^{-4}$	$1.44 [1.38 - 1.54] \times 10^{-4}$
Ri_g	1.15 [†]	1.03	6.43	5.60	4.3	3.7
ϵ [W kg $^{-1}$]	$1.22 [0.83 - 2.27] \times 10^{-7}$ 6.52×10^{-9} [†]	$1.62 [1.14 - 2.59] \times 10^{-5}$ 8.80×10^{-8}	$1.71 [1.18 - 2.86] \times 10^{-8}$ 3.35×10^{-9}	$1.96 [1.50 - 2.43] \times 10^{-6}$ 7.73×10^{-8}	$2.17 [1.83 - 2.70] \times 10^{-8}$ 2.18×10^{-9}	$0.82 [0.55 - 1.41] \times 10^{-6}$ 4.25×10^{-8}
χ [K 2 s $^{-1}$]	$1.19 [0.90 - 1.74] \times 10^{-6}$ 1.36×10^{-8} [†]	$1.73 [1.30 - 2.41] \times 10^{-6}$ 8.64×10^{-8}	$4.38 [2.44 - 8.90] \times 10^{-7}$ 1.37×10^{-8}	$1.10 [0.94 - 1.42] \times 10^{-5}$ 3.41×10^{-7}	$5.40 [3.98 - 8.76] \times 10^{-7}$ 5.80×10^{-9}	$4.23 [3.69 - 5.09] \times 10^{-6}$ 1.50×10^{-7}
K_T [m 2 s $^{-1}$]	$1.30 [0.63 - 2.76] \times 10^{-3}$ 4.85×10^{-6} [†]	$1.30 [0.51 - 3.03] \times 10^{-3}$ 3.79×10^{-5}	$1.55 [0.63 - 3.99] \times 10^{-5}$ 2.61×10^{-7}	$1.58 [0.75 - 5.28] \times 10^{-4}$ 1.33×10^{-5}	$1.39 [1.12 - 1.92] \times 10^{-5}$ 3.08×10^{-7}	$3.52 [3.10 - 4.37] \times 10^{-5}$ 7.33×10^{-6}
R_f	0.137 [0.133 – 0.141]	0.092 [0.083 – 0.099]	0.068 [0.064 – 0.073]	0.081 [0.075 – 0.087]	0.053 [0.052 – 0.054]	0.052 [0.050 – 0.055]
L_T [m]	0.342 [0.333 – 0.350]	0.235 [0.225 – 0.245]	0.099 [0.093 – 0.103]	0.115 [0.110 – 0.123]	0.283 [0.273 – 0.292]	0.222 [0.212 – 0.230]
L_O [m]	0.195 [0.187 – 0.210]	1.35 [1.20 – 1.85]	0.028 [0.027 – 0.032]	0.23 [0.20 – 0.26]	0.058 [0.0558 – 0.062]	0.226 [0.214 – 0.240]
Frr	0.63 [0.62 – 0.64]	2.63 [2.48 – 2.91]	0.52 [0.51 – 0.53]	1.76 [1.66 – 1.88]	0.40 [0.400 – 0.41]	1.19 [1.14 – 1.23]
Re_T	1093 [1009 – 1205]	1716 [1482 – 2300]	85 [78 – 94]	321 [290 – 370]	343 [320 – 365]	548 [510 – 586]
Re_b	1961 [1271 – 3462]	160189 [102140 – 271970]	57 [31 – 141]	4002 [2828 – 5677]	113 [95 – 149]	1699 [1454 – 2079]

Mean values [95% confidence intervals in brackets], and/or median values ([†]) for the three sampling periods (I01, I02 and I03) and for times of biophysical and geophysical turbulence. Unless indicated, the averaging was performed over the 10–25 m depth range. The number of segments in which turbulent quantities were calculated, and were unaffected (n_{good}) or affected (n_{impacts}) by impacts against the instrument, are indicated. The affected data were discarded and not used for computing averages. N^2 is the buoyancy frequency (a measure of stratification); sh^2 , the vertical shear of the horizontal velocity; $Ri_g = N^2/sh^2$, the gradient Richardson number; ϵ the turbulent kinetic energy dissipation rate; χ , the thermal variance dissipation rate; K_T , the turbulent heat diffusivity; R_f , the flux Richardson number or mixing efficiency; L_T , the Thorpe scale; L_O , the Ozmidov scale; Frr , the turbulent Froude number; Re_T , the turbulent Reynolds number; and Re_b the buoyancy Reynolds number.

Extended Data Table 2 | Anchovy development stages

Stage	Stageing	Elapsed time [hours]	Description	Images
F1	I	0	Cell division has not begun. The cytoplasm of the single cell appears as a clear hemisphere at one pole, although may be displaced to other locations. Unfertilized eggs are included in this stage.	
F2	II	4.3	Cell division starts. The blastodisc has a mulberry-like appearance. Blastula cells are very small, but it is possible to distinguish them.	
F3	III	14.3	The eggs have appearance of tissue rather than a collection of individual cells. The segmentation cavity is visible. The blastodermal cap is ≤ 1/3 of the yolk mass.	
F4	IV-VI	31.5	The blastodermal cap is > 1/3 of the yolk mass. There is a rapid differentiation at this stage. At the end of this stage the angle between the tail and the yolk is ≥ 90°	
F5	VII-IX	48.3	The tip of the tail is free from the yolk. At the end of this stage, the curvature of the tail is evident and the gut is apparent along the ventral surface of the tail.	
F6	X-XI	59.3	The free portion of the tail is considered to extend from the body and not from the fold. The tail length is ≥ 3/4 of the yolk-sac. At the end of this stage hatching takes place.	

Development stages of the European anchovy (*Engraulis encrasicolus*) eggs considered in the present work (F1 to F6), equivalence with the stages proposed in ref. ⁵⁶ (Stageing) (I to XI), elapsed time since spawning according to ref. ⁴⁷ for a reference ambient temperature of 17°C, description of the development of the embryo, according to Table A1.3 from ref. ⁴⁰, and images of development stages (F1 to F6) (scale bars are 0.5 mm length).